POLITECNICO DI TORINO
Repository ISTITUZIONALE

Coexistence of Plasmoid and Kelvin-Helmholtz Instabilities in Collisionless Plasma Turbulence

(Article begins on next page)

18 April 2024

Coexistence of Plasmoid and Kelvin–Helmholtz Instabilities in Collisionless Plasma Turbulence

Dario Borgogno[1] , Daniela Grasso[1] , Beatrice Achilli[2], Massimiliano Romé[3] , and Luca Comisso[4]
[1] Istituto dei Sistemi Complessi—CNR and Dipartimento di Energia, Politecnico di Torino, Torino, Italy; daniela.grasso@polito.it
[2] Dipartimento di Fisica, Università degli Studi di Milano, Milano, Italy
[3] Dipartimento di Fisica, Università degli Studi di Milano and INFN Sezione di Milano, Milano, Italy
[4] Department of Astronomy and Columbia Astrophysics Laboratory, Columbia University, New York, New York 10027, USA

Abstract

The plasmoid formation in collisionless plasmas, where magnetic reconnection within turbulence may take place driven by the electron inertia, is analyzed. We find a complex situation in which, due to the presence of strong velocity shears, the typical plasmoid formation, observed to influence the energy cascade in the magnetohydrodynamic context, has to coexist with the Kelvin–Helmholtz (KH) instability. We find that the current density layers may undergo the plasmoid or the KH instability depending on the local values of the magnetic and velocity fields. The competition among these instabilities affects not only the evolution of the current sheets, that may generate plasmoid chains or KH-driven vortices, but also the energy cascade, that is different for the magnetic and kinetic spectra.

1. Introduction

Magnetic reconnection, a fundamental process in magnetized plasmas, involves a topological change in magnetic fields. It is often associated with significant magnetic energy release and is ubiquitous in several astrophysical environments where, due to high Reynolds numbers, the transition to turbulence is unavoidable (Lazarian et al. 2015). In the presence of strong turbulence in the medium, magnetic field line reconnection is continuously met along the flow. This makes magnetic reconnection an intrinsic element of the turbulent cascade and vice versa (Servidio et al. 2009, 2011). Both of these processes involve the transfer of energy across different scales. Magnetic reconnection typically occurs where intense current sheets form, giving rise to plasmoid formation, while the turbulent cascade explains how the energy provided at large scales is dissipated at small scales. The strong interplay between these two processes is an essential aspect of the energy cascade, and indeed significant efforts have been devoted to understanding how the reconnection process, via plasmoid instability, influences the turbulent cascade in resistive magnetohydrodynamics (MHD) (Biskamp & Welter 1989; Politano et al. 1989; Carbone et al. 1990; Carbone 1995; Politano et al. 1995; Boldyrev & Loureiro 2017; Mallet et al. 2017; Comisso et al. 2018; Dong et al. 2018).

The first analytical calculation of the impact of the plasmoid formation on the MHD turbulent cascade was performed by Carbone et al. (1990), who proposed that current sheets break apart when $\gamma\tau_{\mathrm{nl}} \sim 1$, with τ_{nl} and γ corresponding to the nonlinear eddy turnover time and the growth rate of the fastest tearing mode, respectively. Under this condition, they derived a length scale at which the inertial range of turbulence breaks and found that the energy spectrum steepens because of the plasmoid instability. The same disruption condition was employed in Boldyrev & Loureiro (2017) and Mallet et al. (2017), where similar predictions were obtained. A refined theory was developed in Comisso et al. (2018) by taking into account that plasmoids disrupt the current sheet when $\gamma\tau_{\mathrm{nl}} \gg 1$ rather than $\gamma\tau_{\mathrm{nl}} \sim 1$ (Comisso et al. 2016, 2017; Huang et al. 2017, 2019; Baty 2020). Then, the theoretical predictions were confirmed by the high-resolution MHD turbulence simulations of Dong et al. (2018).

However, space and astrophysical plasmas where reconnection and turbulence have mutual influence are most of the time collisionless (Ji & Daughton 2011), suggesting that the electron inertia may play a crucial role as a driving mechanism for reconnection. Indeed the plasmoid instability in collisionless regimes of plasma turbulence has started to be investigated also numerically via particle-in-cell (Comisso & Sironi 2018, 2019) and hybrid Vlasov–Maxwell simulations (Cerri & Califano 2017; Franci et al. 2017). Nonetheless, to benefit of the advantages of a fluid description, a two-fluid model can be adopted. In the framework of collisionless magnetic reconnection described by two-fluid equations, several studies have also been devoted to the evolution of current and vorticity sheets that undergo secondary instabilities of the fluid type, especially the Kelvin–Helmholtz (KH) instability (Del Sarto et al. 2003; Grasso et al. 2007, 2009). For the limiting case of symmetric equilibrium magnetic field configurations, these studies found that the KH instability could develop only when the ion sound Larmor radius was smaller than the electron inertial length. More recently (Grasso et al. 2020), it has been shown that this condition is wiped out when asymmetric equilibrium magnetic field configurations are considered. Notwithstanding, the competition of the plasmoid and KH instabilities and their combined effect on the collisionless turbulent cascade remains largely unexplored. On the other hand, the linear interplay of these two instabilities in the resistive regime is a textbook subject (Biskamp 2000). Indeed, it is known that the presence of a shear flow together with a magnetic shear leads to an

increase in the linear growth rate as well as of the number of modes growing due to tearing instability. More recently, the coexistence of the plasmoid instability together with the KH one has been studied in the framework of a resistive Sweet–Parker current sheet linear model (Loureiro et al. 2013).

As a contribution toward the clarification of the influence of magnetic reconnection on the turbulent cascade, here we analyze the development of plasmoids in a turbulent collisionless plasma where the reconnection mechanism is provided by the electron inertia. We find that the presence of strong shear flows, naturally generated in the turbulent plasma, also drives the KH instability that competes with the plasmoid instability. The impact of the current sheets disruption on the energy cascade is addressed, together with the influence of the KH instability on the reconnection growth rate. A comparison between resistive and collisionless plasmoid formation is performed to understand the main differences between these two regimes.

2. Model Equations and Numerical Approach

We consider a reduced two-dimensional, two-fluid model suitable to describe magnetic reconnection in weakly collisional regimes (Grasso et al. 1999). This model retains microscopic effects related to the finite electron inertia in a simplified fluid framework and therefore allows to reduce the competition of the plasmoid and KH instabilities to a few essential ingredients. In view of this, here we consider, as a first step, the vanishing electron temperature limit of the model. The equations for the magnetic flux and the stream function, normalized to the Alfvén time, evaluated using the superimposed transverse magnetic field and the box length, are

$$\frac{\partial \psi}{\partial t} + [\varphi, \psi] = -d_e^2 \frac{\partial J}{\partial t} - d_e^2 [\varphi, J] - \eta(J - J_{\mathrm{eq}}), \quad (1)$$

$$\frac{\partial U}{\partial t} + [\varphi, U] = [J, \psi] + \nu \nabla^2 U, \quad (2)$$

where η is the plasma resistivity, ν is the kinematic viscosity, $d_e = c/\omega_{\mathrm{pe}}$ is the electron skin depth, with c and ω_{pe} indicating the speed of light and the plasma frequency, respectively. Furthermore, $J = -\nabla^2 \psi$ is the electric current density, and $U = \nabla^2 \varphi$ is the plasma vorticity. The magnetic and velocity fields are given by $\boldsymbol{B} = B_0 \boldsymbol{e}_z + \nabla \psi \times \boldsymbol{e}_z$ and $\boldsymbol{v} = \boldsymbol{e}_z \times \nabla \varphi$, where B_0 is a strong (with respect to the in-plane component) uniform magnetic field. Note that, due to the adopted normalization and the dependence of the Alfvén velocity on B_0, the amplitudes of the magnetic and velocity fields are directly comparable. Equations (1)–(2) are solved with a parallel code based on a pseudospectral discretization method, where spatial derivatives are evaluated in the Fourier space. The time stepping is performed in real space with a third-order Adams–Bashforth scheme.

2.1. Setup and Convergence Tests

We adopt the initial condition setup considered in Dong et al. (2018). We solve Equations (1)–(2) in the domain $-1/2 \leqslant x, \ y \leqslant 1/2$. For the collisionless runs, the plasma resistivity is set to $\eta = 0$, while the viscosity, introduced for numerical reasons, has been fixed to $\nu = 10^{-6}$. The electron skin depth is set to $d_e = 5 \times 10^{-4}$ in order to achieve a large scale separation. We initialize the simulation placing

uncorrelated, equipartitioned ψ and φ fluctuations in Fourier harmonics

$$\psi = -\sum \psi_{0mn} \sin(k_m x + \xi_{1mn}) \sin(k_n y + \xi_{2mn}), \quad (3)$$

$$\varphi = \sum \varphi_{0mn} \sin(k_m x + \xi_{3mn}) \sin(k_n y + \xi_{4mn}), \quad (4)$$

where m and n indicate the mode numbers in the x and y directions, $k_m = 2\pi m/L$ are the wavenumbers, and ξ_i, where $i = 1, \ldots, 4$, are random phases. Energy is initialized in the range $m, n = 0, \ldots, 10$, with $l_{\min} \leqslant (m^2 + n^2)^{1/2} \leqslant l_{\max}$, where $l_{\min} = 1$, $l_{\max} = 10$ and

$$\psi_{0mn} = \psi_0 \Big/ 2\pi \sqrt{(m^2 + n^2)(l_{\max}^2 - l_{\min}^2)}, \quad (5)$$

$$\varphi_{0mn} = \varphi_0 \Big/ 2\pi \sqrt{(m^2 + n^2)(l_{\max}^2 - l_{\min}^2)}. \quad (6)$$

This is essentially equivalent to set 10 large eddies per side, and this is convenient both to achieve early an adequate state of turbulence and to have thin and elongated current sheets with a high aspect ratio $l_{\mathrm{cs}}/d_e \sim 200$. Namely, these conditions are necessary to see the onset of the plasmoid instability (Comisso & Sironi 2018, 2019). On the other hand, the length of the largest current sheets is related to the size of the largest eddies for geometrical reasons, and the size of the largest eddies is related to the box size. So, if we perturb 10 initial modes, it results to $l_{\mathrm{cs}} \sim 1/10$. We set $\varphi_0 = \psi_0 \simeq 2$ in order to have initial energy $E = \frac{1}{2}\langle v^2 + \boldsymbol{B}^2 \rangle \simeq \frac{1}{8}(\varphi_0^2 + \psi_0^2) \simeq 1$, where $\langle \cdots \rangle$ represents the spatial average.

The convergence of our results has been checked analyzing the rms value of the current density, shown in the left panel of Figure 1, on three runs with increasing resolution: with 9600^2, $19{,}040^2$, and $38{,}080^2$ grid points. Convergence is reached starting from $19{,}040^2$ grid points. As complementary information, in the right panel of Figure 1, we show the rms of the vorticity, equivalently adopted as an indicator of convergence in resistive MHD turbulence. However, in collisionless systems this quantity has a different behavior. The electron skin depth provides the physical mechanism that limits the current density, which, despite the scales developed well below d_e, remains mainly distributed over d_e (Grasso et al. 1999). On the contrary, the viscosity does not prevent the cascade toward smaller scales. Indeed in analogous works carried out in the resistive regime (Dong et al. 2018) the values of resistivity and viscosity were acting on the same scales allowing to reach convergence on the rms of both the current density and the vorticity. The different behavior of the vorticity provides the justification for focusing on the highest-resolution run from now on.

We will refer to the time at which the rms of the current density reaches its peak as t_{peak}, which should represent the maximum turbulent activity (Mininni & Pouquet 2009). The simulations carried out with lower resolution, up to 9600^2 grid points, have shown that $t_{\mathrm{peak}}/\tau_{\mathrm{nl}} \approx 6$ and does not depend on the numerical grid. However, as is shown in Figure 1, we stopped the high-resolution run before reaching t_{peak} because, as we discuss later in the paper, the plasmoid formation starts well in advance of it.

3. Plasmoid Formation

Although plasmoids have been already detected in several other collisionless turbulence works (Cerri & Califano 2017; Franci et al. 2017; Comisso & Sironi 2018, 2019; Comisso et al. 2020),
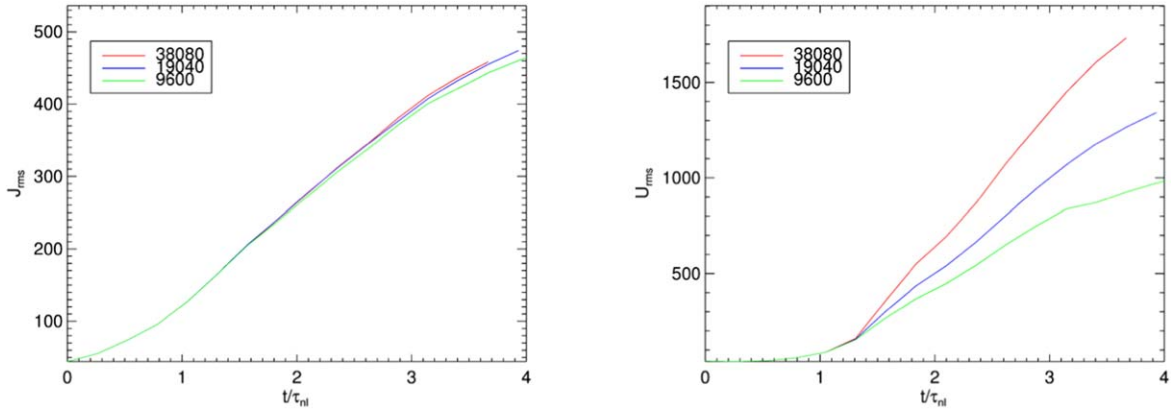
Figure 1. rms value of the current density and vorticity for increasing resolutions.
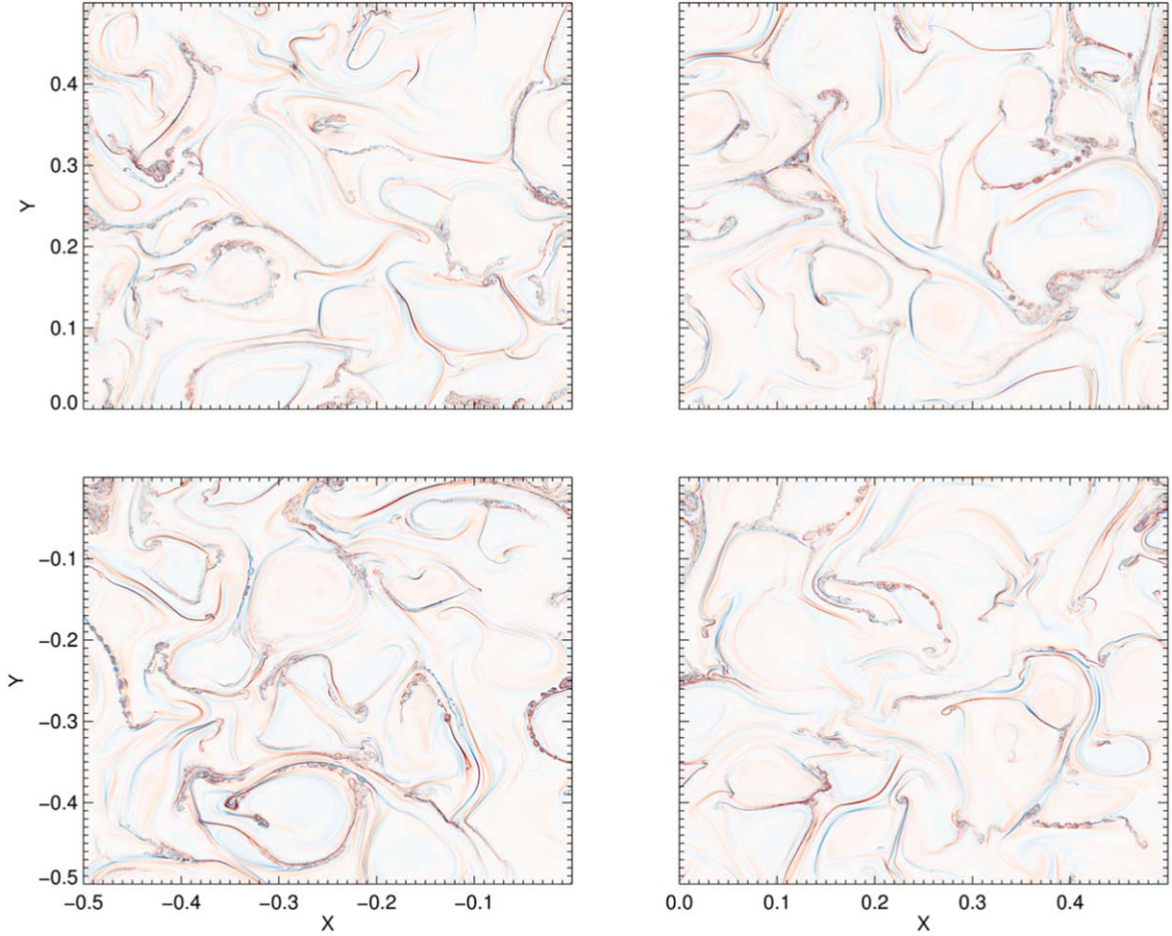

Figure 2. J over the entire simulation domain at $t/\tau_{nl} = 2.62$.

their competition with the KH instability was, as far as we know, never reported.

We start considering the time evolution of the J field over the entire simulation domain. In Figure 2, where the domain has been divided in four subdomains, we can see that the initial eddies merge, giving rise to the formation of thin and elongated current sheets, which are analogous for the vorticity. Zooming in and superimposing the contour levels of the magnetic flux, we can distinguish between the different evolution of these current sheets, which may be dominated by the plasmoid or KH instability. In Figure 3, the contour levels of ψ clearly indicate

the presence of plasmoid chains in each of the subdomains of Figure 2. However, it is possible to also observe current sheets dominated by the KH instability, where no magnetic structures are detected. We point out that, if on one hand the time evolution of the plasmoid-dominated current sheets ends up with the generation of turbulence, on the other hand the KH-dominated current sheets never show the presence of plasmoids. Nonetheless, it is likely that the turbulent evolution of these sheets also generates secondary reconnection sites (Faganello et al. 2008), as also revealed by the X-point detection, not shown here, but these are not related to the
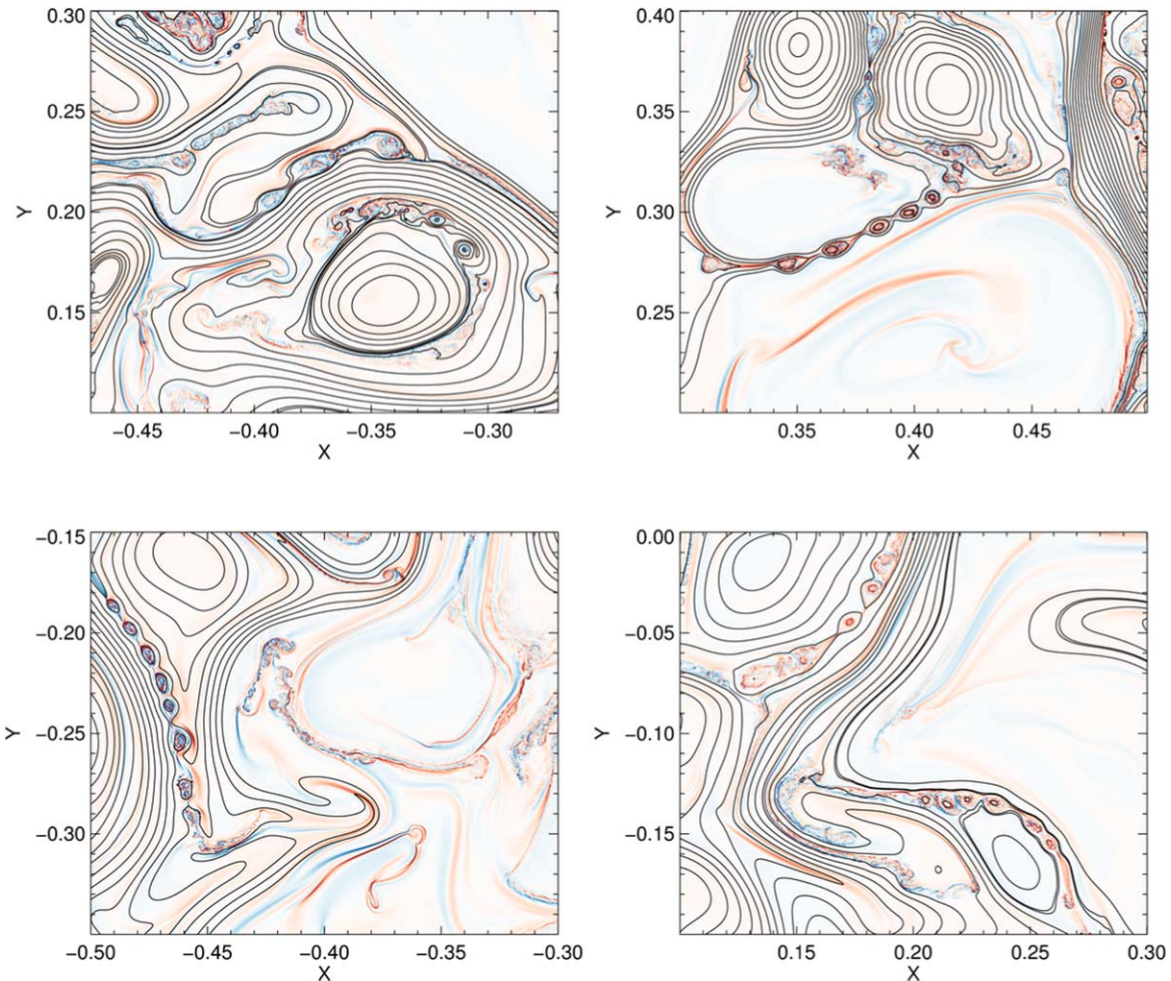
3

Figure 3. Zoomed-in regions of the domain in which J, at $t/\tau_{\rm nl} = 2.62$, is plotted with the corresponding magnetic surfaces, highlighting the plasmoid chains.

plasmoid instability. Notice that we also had hints of plasmoid formation in the runs with lower resolution, from which we have been able to tell that this phenomenon happens before reaching $t_{\rm peak}$, which is why we stopped our highest-resolution run earlier.

This early appearance of the plasmoid instability brings the fast disruption of the current sheets. In fact, the proliferation of plasmoids is accompanied by an increasing number of small vortices, sometimes making the distinction between the two difficult. As we show in the Appendix, the presence of a sheared velocity field enhances significantly the growth rate of the reconnecting mode in the collisionless case, compared to the resistive one. In order to understand the reason of the different evolution of the current sheets, we analyze first the intense current density layer, which leads to the formation of the plasmoid chain in the left bottom panel of Figure 3. In Figure 4, the current density sheet is shown at $t/\tau_{\rm nl} = 2.1$, right before its disruption, together with the profiles of the component of the velocity and magnetic fields in the direction parallel to the layer on a perpendicular cross section.

These profiles resemble the standard equilibrium shape of the velocity and magnetic field, like the ones treated in the Appendix. Here it is important to observe that the magnetic field amplitude on the layer boundary is greater than the velocity peak, located at the maximum of the current sheet. According to the linear theory of shear flow instability (Biskamp 2000) this is a stabilizing condition for the KH

instability. Indeed, the layers evolve forming the plasmoid chain discussed above. A similar approach, although in the context of resistive MHD, was adopted also in Loureiro et al. (2013).

We consider now a different current density layer at $t/\tau_{\rm nl} = 2.1$, which has evolved according to the KH instability as shown in Figure 3 at $t/\tau_{\rm nl} = 2.62$. The magnetic field and velocity profiles along the layers, shown in Figure 5, are now in an opposite relation: the velocity peak significantly exceeds the magnetic field amplitude, and the current sheet is disrupted under the effects of a fluid-type instability. To highlight the difference with respect to the layers that evolve according to the plasmoid instability, in Figure 6 we show the evolution of the vorticity layer that corresponds to the current density one analyzed in Figure 5. In the left panel, the vorticity layer at $t/\tau_{\rm nl} = 2.36$ has started to develop the KH instability that leads to its complete disruption in many small vortices at time $t/\tau_{\rm nl} = 2.62$, as shown in the right panel.

Finally, Figure 7 shows an example of how turbulence develops in the regions where current sheets undergo the plasmoid instability, as anticipated at the beginning of this section. Here the evolution of the vorticity sheet corresponding to the current sheet shown in Figure 4 is plotted at two subsequent times. In the first stages of the instability (left frame), turbulence is bounded inside the magnetic structures, where the vorticity and current density exhibit small scale vortices. This is a distinguished feature of the vanishing
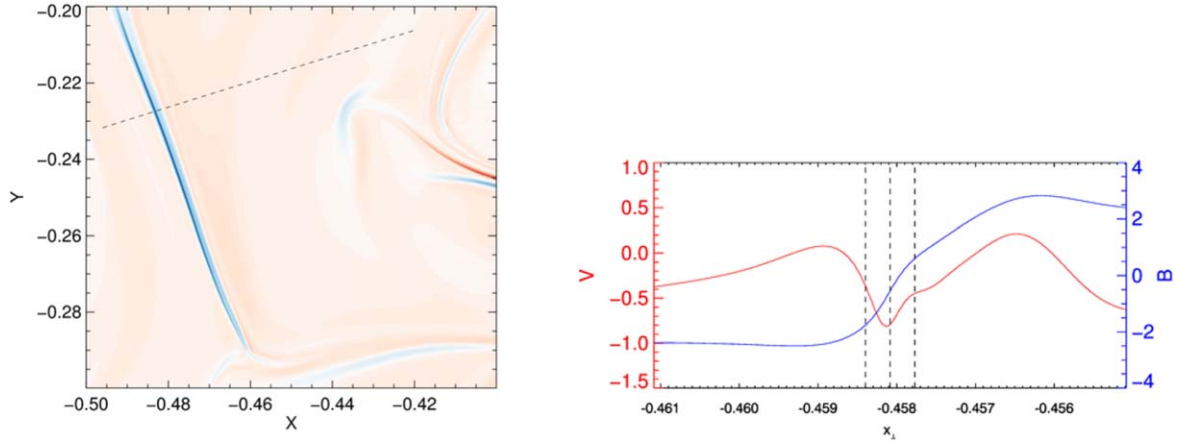
Figure 4. Left: contour plot of J at $t/\tau_{nl} = 2.1$. The dashed overplotted line identifies the direction perpendicular to the current sheet at the point $(-0.483246, -0.227442)$. Right: velocity and magnetic field components along the direction parallel to the current sheet at the same point vs. the coordinate of the perpendicular cross section shown in the left frame. The outer vertical dashed lines identify the boundaries of the current layer, while the central one marks the position of the peak of the current sheet.
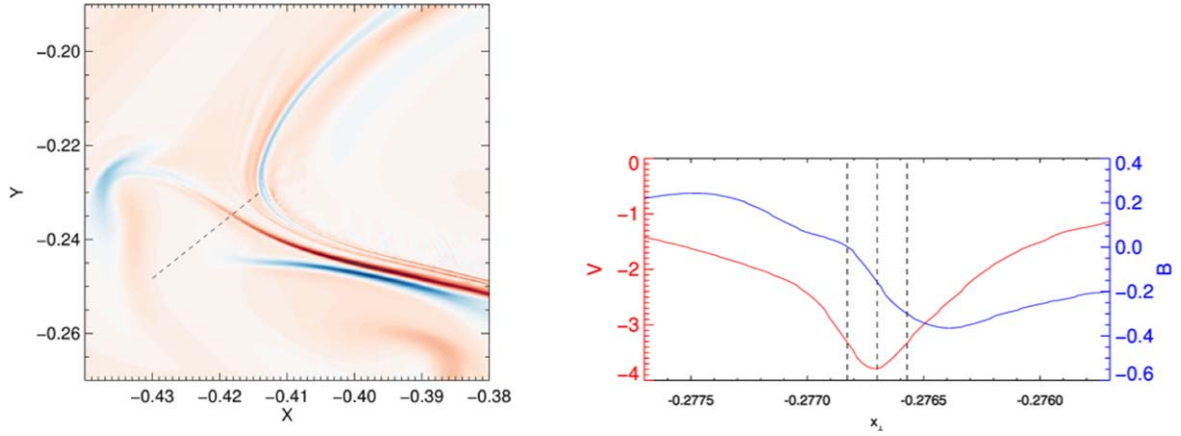

Figure 5. As in Figure 4, but in a different subdomain. The considered point is $(-0.418172, -0.234743)$.
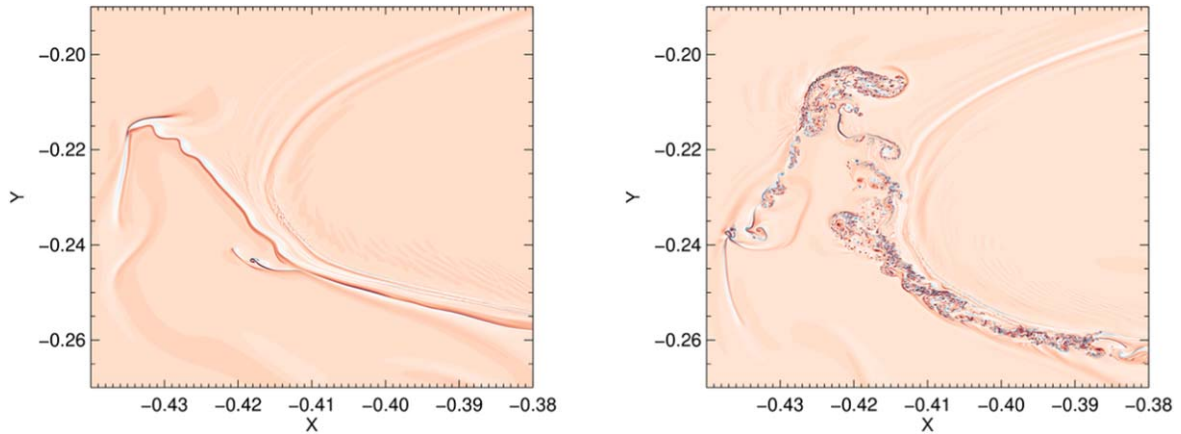

Figure 6. Two different stages of the nonlinear evolution of a vorticity layer shown via $U = \nabla^2\varphi$, which, starting from a laminar structure at $t/\tau_{nl} = 2.1$, develops a KH instability at $t/\tau_{nl} = 2.366$ (left panel) ending in a turbulent structure at $t/\tau_{nl} = 2.62$ (right panel).

electron temperature collisionless regimes that has also been observed in purely magnetic reconnection numerical simulations (Del Sarto et al. 2003; Grasso et al. 2007). When the plasmoids become larger (right frame), their mutual interaction leads to the coalescence between the magnetic structures that belong to the same island chain. This results in large turbulent regions where the magnetic structures eventually disappear. The magnetic connections between the nearby turbulent regions finally drive the appearance of macroscopic turbulent domains.
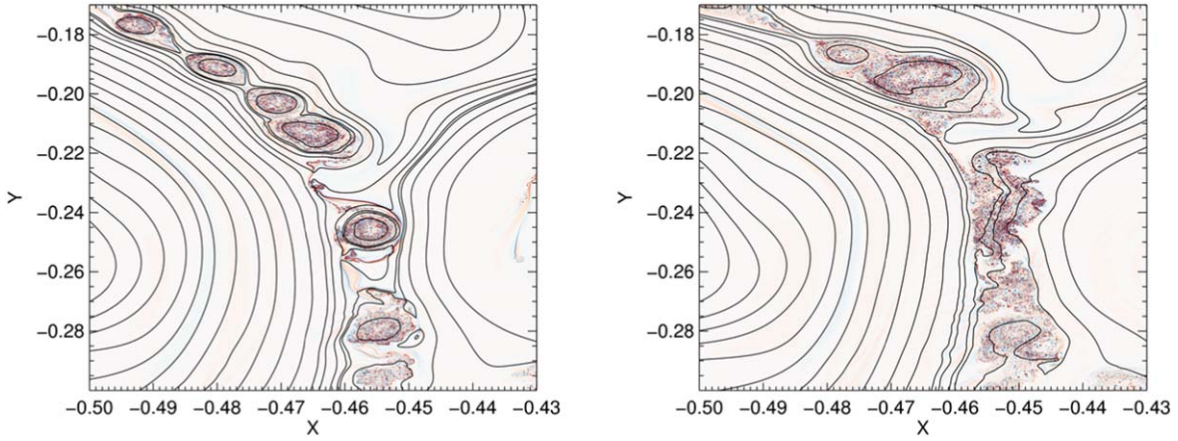
Figure 7. Vorticity distribution at two different stages of the nonlinear evolution of the current sheet shown in Figure 4. The overplotted black lines show the corresponding magnetic structures through isocontours of the magnetic flux ψ. The set of figures highlights the transition of turbulence from a localized distribution inside the magnetic structures at $t/\tau_{\rm nl} = 2.88$ (left frame), to a macroscopic scale when the coalescence of the plasmoids starts at $t/\tau_{\rm nl} = 3.14$ (right frame).

The layers examined above are representative of the many ones that form and disrupt according either to the plasmoid or the KH instability, depending on the relative magnitude of the magnetic and velocity fields. Although distinguishing between these two different evolution paths may be difficult, we believe that their coexistence is crucial in explaining the energy cascade.

4. Plasmoid-mediated Turbulence in the Collisionless Regime

If the turbulent energy cascade is dominated by the formation of plasmoids, the energy spectrum steepens with respect to the standard inertial range spectrum (Biskamp 2003). We can calculate the half thickness λ of the turbulence-generated current sheets at which the plasmoid instability becomes critical by following Comisso et al. (2018) and Comisso & Sironi (2019). In order to affect the energy cascade, plasmoids need to grow to large amplitude before the current sheets in which they are born are swept away by the turbulent fluctuations. Therefore, the first step of the analysis requires determining the condition for the instability growth rate to amplify a perturbation from noise level to nonlinearity in one eddy turnover time, $\tau_{\rm nl}$. According to Comisso et al. (2016, 2017, 2018), this is equivalent to the condition

$$\ln\left(\frac{\delta_{\rm in}}{w_0}\right) = \frac{\gamma \tau_{\rm nl}}{2}, \qquad (7)$$

where $\delta_{\rm in}$ is the half width of the inner tearing layer. For the collisionless regime of interest here, we can take $\delta_{\rm in} = d_e$ (Ottaviani & Porcelli 1995). Furthermore, $w_0 = 2(\psi_0 \lambda/\delta b_\lambda)^{1/2}$ is the half width of the plasmoid, where δb_λ indicates the magnetic field fluctuation at scale λ. The quantity $\psi_0 = \kappa(k_\xi \xi)^{-\alpha}$ is the noise perturbation, which is assumed to have a general power-law form. Here, κ is the noise amplitude, ξ is the half length of the current sheet, k_ξ is the wavenumber along the ξ direction, and α is the power-law exponent, which has to be self-consistently determined from the turbulent energy spectrum.

We can substitute the growth rate of the dominant collisionless tearing mode into Equation (7) and rewrite this

expression as (Comisso et al. 2016)

$$\ln\left(\frac{\delta_{\rm in}}{w_0}\right) = \frac{1}{2}\int_{\lambda_0}^{\lambda_d} \gamma(\lambda)\frac{dt}{d\lambda}d\lambda, \qquad (8)$$

where $\gamma = \gamma_s \gamma_l/(\gamma_s + \gamma_l)$ is the semiharmonic mean of the growth rates γ_s and γ_l, which characterize the small and large Δ' regimes, respectively (Ottaviani & Porcelli 1995), and suffix d denotes current sheet disruption. Here, Δ' is the tearing stability parameter (Furth et al. 1965), which, for a Harris-like (Harris 1962) current sheet, can be evaluated as (White 1986)

$$\Delta' = \frac{2}{\lambda}\left(\frac{1}{k_\xi \lambda} - k_\xi \lambda\right). \qquad (9)$$

Equation (8) should be solved for an exponentially shrinking current sheet of the form $\lambda(t) = \lambda_0 e^{-t/\tau}$, using also $\lambda_d \ll \lambda_0$ and the fact that $k_\xi \lambda \ll 1$ for the plasmoids that disrupt the current sheet. Then we notice that the wavenumber and the growth rate of the plasmoids at current sheet disruption have the same scaling properties of the fastest collisionless tearing mode (Comisso & Sironi 2019), and can be written as

$$k_{\xi,d} \sim \frac{d_e}{\lambda_d^2}, \qquad \gamma_d \sim \frac{d_e^2}{\lambda_d^3}v_{A_\lambda}, \qquad (10)$$

where v_{A_λ} is the Alfvén speed associated with the fluctuating magnetic field at scale λ.

Solving Equation (8) for the dominant collisionless tearing mode, we obtain the following expression for the critical aspect ratio of the current sheets (Comisso & Sironi 2019)

$$\frac{\lambda_d}{\xi} \sim \left(\frac{d_e}{\xi}\right)^{2/3}\left[\ln\left(\frac{1}{2\hat{\kappa}^{1/2}}\left(\frac{d_e}{\xi}\right)^{1+\alpha/2}\left(\frac{\xi}{\lambda_d}\right)^{1/2+\alpha}\right)\right]^{-1/3}, \qquad (11)$$

where $\hat{\kappa} = \kappa/\delta b_\lambda \xi$ is the normalized amplitude of the noise that seeds the plasmoid instability. Here, we set $\tau = 1$ as we consider current sheets forming on the Alfvénic timescale. Equation (11) can be solved by iteration (Comisso & Sironi 2019), replacing into Equation (11) the solution at the

zeroth order. Thus, at the first order, one has

$$\lambda_d \sim d_e^{2/3} \xi^{1/3} \left[\ln \left(\frac{1}{2\hat{\kappa}^{1/2}} \left(\frac{d_e}{\xi} \right)^{(4-\alpha)/6} \right) \right]^{-1/3}, \qquad (12)$$

while the growth rate at the end of the linear phase is

$$\gamma_d \tau_{\mathrm{nl}} \sim \ln \left[\frac{1}{2\hat{\kappa}^{1/2}} \left(\frac{d_e}{\xi} \right)^{\frac{4-\alpha}{6}} \right]. \qquad (13)$$

From this relation we have that $\gamma_d \tau_{\mathrm{nl}} \gg 1$ at current sheet disruption, as is required for the instability to amplify the perturbation to a significant level within the lifetime of the current sheet.

In order to determine the energy spectrum in the plasmoid-dominated range, we consider a constant energy flux $\varepsilon = \delta b_\lambda^2 / \tau_{\mathrm{nl}}$, where the nonlinear timescale is now controlled by the growth rate given by Equation (13). Therefore, using

$$\tau_{\mathrm{nl}} \sim \frac{1}{\gamma_d} \ln \left[\frac{1}{2\hat{\kappa}^{1/2}} \left(\frac{d_e}{\xi} \right)^{\frac{4-\alpha}{6}} \right]$$

$$\sim \frac{\lambda_d^3}{d_e^2} \frac{1}{\delta b_\lambda} \ln \left[\frac{1}{2\hat{\kappa}^{1/2}} \left(\frac{d_e}{\xi} \right)^{\frac{4-\alpha}{6}} \right], \qquad (14)$$

we obtain

$$\delta b_\lambda \sim \frac{\varepsilon^{1/3} \lambda_d}{d_e^{2/3}} \left[\ln \left(\frac{1}{2\hat{\kappa}^{1/2}} \left(\frac{d_e}{\xi} \right)^{\frac{4-\alpha}{6}} \right) \right]^{1/3}. \qquad (15)$$

The expression of δb_λ as a function of λ in the plasmoid-dominated range can be obtained following the same first-order approximation adopted in Comisso et al. (2018) and using the results obtained so far in the collisionless regime.

As a first step, we need to adopt a suitable expression of ξ as a function of λ, as well as determine α and $\hat{\kappa}$. The first task can be easily carried out neglecting the logarithm to obtain a zeroth order estimate of the noise and considering λ_d as a fixed scale in the previous equations for τ_{nl} and δb_λ. Hence, if we introduce the alignment angle sine $\sin \vartheta_\lambda \sim \lambda/\xi$, we obtain

$$\sin \vartheta_\lambda \sim \left(\frac{\lambda}{\lambda_d} \right)^{-2} \left(\frac{\lambda_d}{L} \right)^{-2} \left(\frac{d_e}{L} \right)^2 \qquad (16)$$

and

$$\xi \sim \left(\frac{\lambda}{\lambda_d} \right)^3 \left(\frac{\lambda_d}{L} \right)^3 \left(\frac{d_e}{L} \right)^{-2} L, \qquad (17)$$

as from Equation (15) we have $\delta b_\lambda \propto \lambda$, $\delta b_\lambda \propto k_\xi^{-1/3}$. This implies that at the zeroth order $E(k_\xi) \propto k_\xi^{-5/3}$ and considering that $E(k_\xi) \sim \psi_0^2 k_\xi = (\kappa^2/\xi)(k_\xi \xi)^{1-2\alpha}$ we can determine $\alpha = 4/3$. To evaluate $\hat{\kappa}$ in a consistent way, we take into account the energy content at a given scale, δb_λ^2, the probability of occurrence of a certain fluctuation amplitude on the current sheet, f, and the projection of the fluctuation onto the unstable modes, $\delta_{\mathrm{in}}/\lambda$, as (Comisso et al. 2018)

$$\kappa \sim f \delta b_\lambda \xi \left(\frac{\delta_{\mathrm{in}}}{\lambda} \right), \qquad (18)$$

where $\delta b_\lambda \xi$ is the magnetic flux associated with the energy content at a scale λ. Factor f can be estimated from geometrical considerations. Indeed, if we envision current sheets that form between alternately twisted flux bundles (magnetic islands), a close-packed configuration yields hexagonal arrays with current sheets that develop on two of the six edges (see, e.g., Zhou et al. 2014). Therefore, from the area of a regular hexagon, we can estimate $f \sim c_s \lambda/\xi$, with $c_s = 2/(3\sqrt{3})$. Then, the noise that seeds the plasmoid instability can be estimated as

$$\hat{\kappa} \sim c_s \frac{\delta_{\mathrm{in}}}{\xi} \sim c_s \left(\frac{\lambda}{\lambda_d} \right)^{-3} \left(\frac{\lambda_d}{L} \right)^{-3} \left(\frac{d_e}{L} \right)^3. \qquad (19)$$

We can now substitute $\alpha = 4/3$ and Equation (19) into Equation (15) obtaining

$$\delta b_\lambda \sim \frac{\varepsilon^{1/3} \lambda_d}{d_e^{2/3}} \left[\ln \left(\frac{1}{2c_s^{1/2}} \left(\frac{\lambda}{\lambda_d} \right)^{1/6} \left(\frac{\lambda_d}{L} \right)^{1/6} \left(\frac{d_e}{L} \right)^{-1/6} \right) \right]^{1/3}. \qquad (20)$$

Finally, the energy spectrum can be obtained from $\int_k^\infty E(k') dk' \simeq (\delta b_\lambda)^2$, which gives us

$$E(k) \sim 2 \frac{\varepsilon^{2/3} k^{-3}}{d_e^{4/3}} \left[\ln \left(\frac{(k_* d_e)^{-1/6}}{2c_s^{1/2}} \left(\frac{k_*}{k} \right)^{1/6} \right) \right]^{2/3}. \qquad (21)$$

We can see that for the considered collisionless plasma model, the turbulence energy spectrum in the plasmoid-dominated range tends to $E(k) \propto k^{-3}$ at the zeroth order. However, the exponential growth rate of the plasmoid instability also results in a nontrivial relationship that does not obey a true power law, as it is reflected by the logarithmic factor. We also notice that, as the adopted plasma model does not include ion physics, the plasmoid-dominated range is not limited by the ion skin depth d_i or the ion Larmor radius ρ_i, but it rather ends at the scale corresponding to the electron skin depth $k_{d_e} \sim 2\pi/d_e$.

4.1. Energy Spectra

We analyze the magnetic and kinetic energy spectra resulting from our simulations in comparison with the analytical prediction derived above. Figure 8 (left frame) shows the curves for the magnetic energy spectra at four times, after the plasmoid formation, together with the theoretical slope values for the inertial and plasmoid range. The change in the slope occurs at $k d_e \sim 0.1$, which corresponds to plasmoids of size $w_{\mathrm{pl}} \sim 0.1 l_{\mathrm{cs}} \sim 20 d_e$, as can also be inferred from the plasmoid chains highlighted in Figure 3. The average values of the slope evaluated on these curves in the two aforementioned ranges are $\gamma_{\mathrm{mag1}} = -1.3$ and $\gamma_{\mathrm{mag2}} = -2.7$. The latter somewhat differs from our theoretical prediction of the slope in the plasmoid-dominated regime in the collisionless case. Indeed, as the time increases, the magnetic energy spectrum tends to flatten, consistent with the observation that the fully plasmoid-mediated regime is somehow inhibited by the presence of a turbulence dominated by the KH instability. In the right frame of Figure 8, an analogous picture is shown for the kinetic energy spectra, whose slope never matches that of the magnetic one in the same regime. The average values of the slopes evaluated on these curves are $\gamma_{\mathrm{kin1}} = -1.14$ and $\gamma_{\mathrm{kin2}} = -1.7$, clearly far from $-3/2$ and -3. Moreover, the kinetic energy
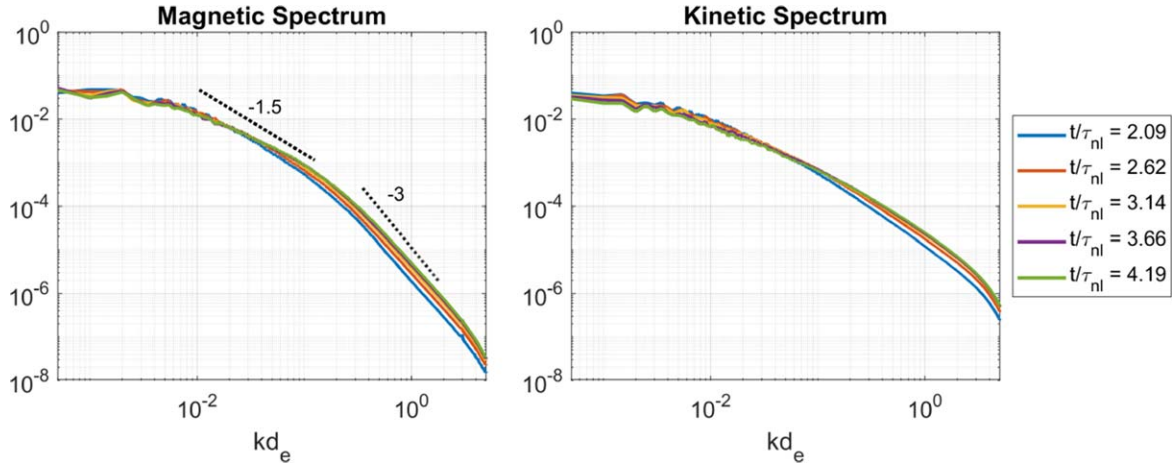
Figure 8. Magnetic and kinetic energy spectra at five different nonlinear times after the plasmoid formation has started.
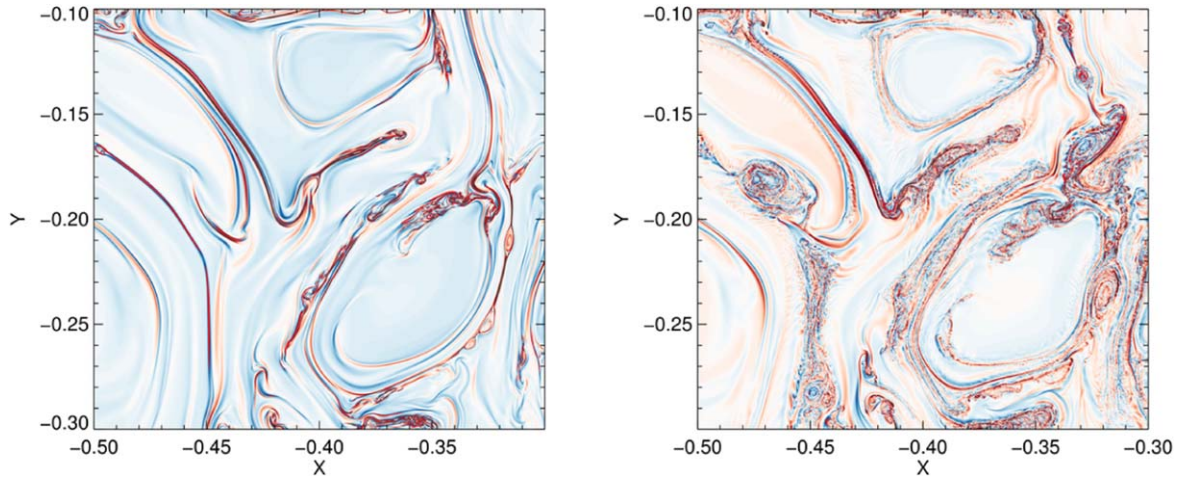

Figure 9. J for the resistive (left) and collisionless (right) simulations around $t/\tau_{\rm nl} = 3.41$.

spectrum changes more smoothly with respect to the magnetic one. While the abrupt change of the cascade to small scales in the magnetic energy spectrum is caused by the generation of the plasmoids, which facilitates the cascade of magnetic energy, the kinetic energy spectrum is dominated by the KH instability that continuously generates smaller and smaller scales due to the low viscosity value adopted here in order not to affect the collisionless dynamics.

4.2. Comparison with a Resistive Case

In order to clarify this issue, we performed a resistive simulation with $19,040^2$ grid points, choosing η such that the inertial ranges of the two simulations are comparable. We estimate the dissipation scale of the resistive simulation as (Servidio et al. 2011)

$$k_{\rm diss}(t) = \left(\frac{\varepsilon}{\nu^3}\right)^{1/4} = \frac{\langle U^2 + J^2\rangle^{1/4}}{\nu^{1/2}}. \qquad (22)$$

Solving this equation for ν and choosing the plasma resistivity to be equal to the plasma viscosity, and further using $k_{\rm diss} = k_{d_e} = 2\pi/d_e$, we obtain

$$\nu_{\rm diss} = \frac{\langle U^2 + J^2\rangle^{1/2}}{(2\pi/d_e)^2}. \qquad (23)$$

We take for η the value of $\nu_{\rm diss}$ at time $t \simeq 2\,\tau_{\rm nl}$, when we detect the development of the plasmoid instability in the previous simulations, so we set $\eta = 5 \times 10^{-6}$.

Looking directly at the current density field evolution, we can spot some differences with respect to the collisionless case. In Figure 9, there is a small number of plasmoids at times at which we could spot numerous plasmoids in the collisionless regime. However, the number of plasmoids significantly increases as we follow the turbulence evolution and we get closer to $t_{\rm peak}$. This difference can be understood according to the linear analysis performed in the Appendix. Indeed, when comparing the resistive and collisionless regimes characterized by the same magnetic dissipation length scale, we find the new interesting result that the impact of a velocity shear on the growth rate of reconnecting modes is greater in the collisionless regime. It turns out that the number of unstable modes increases as well as their growth rate, which doubles that of the resistive regime. Hence, it is reasonable to find that the plasmoid instability starts earlier in the collisionless case. In the resistive regime, the current and vorticity sheets evolve following a laminar behavior and are not affected by the KH instability. Moreover, while in the collisionless regime plasmoids appear to already have grown to a highly nonlinear phase and have fully disrupted the current sheets in which they were formed, in the resistive case we can see the presence of
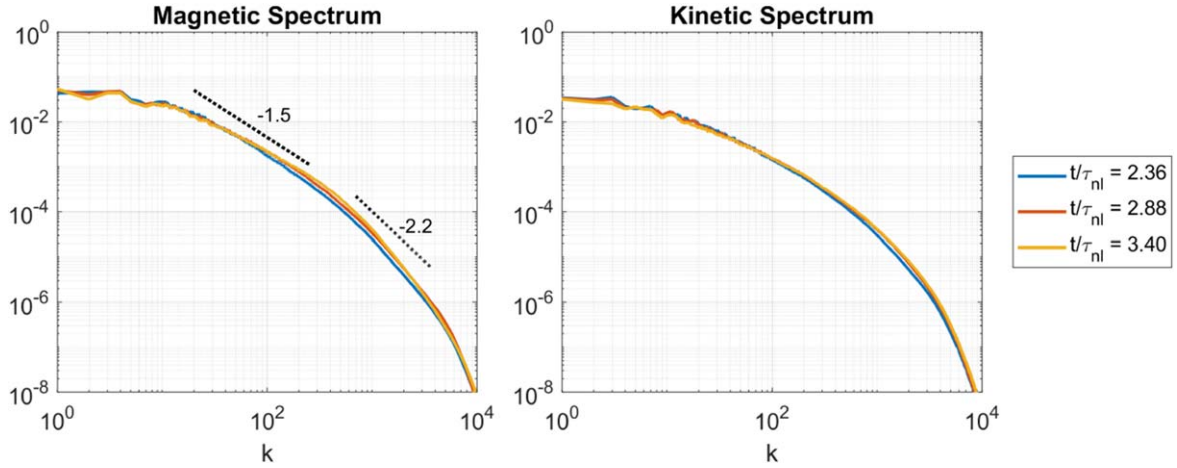
Figure 10. Magnetic and kinetic energy spectra at three different nonlinear times for the resistive case.

laminar current sheets within the first generation of plasmoids. This is not surprising if compared with the results in Dong et al. (2018), where plasmoids were detected with η of the order of 10^{-6}, which is smaller than the value adopted here. This results in less intense resistive current sheets preventing their further thinning to smaller scales.

Figure 10 is the analogous of Figure 8 for the resistive case. Also here, within the inertial range, we are able to identify two different ranges, characterized by different slopes in the magnetic energy spectrum. Even though the slope of the spectrum is varying, it shows a tendency to remain steeper than the slope of -2.2 observed in Dong et al. (2018). This can be ascribed to the fact that in our case the plasmoid instability is still developing, and we might not have reached the plasmoid-mediated regime in which the -2.2 slope is expected to hold. It was not the same in the collisionless regime, where the slope was progressively flattening from the zeroth order theoretical value of -3 after the disruption of current sheets.

The kinetic energy spectrum in the collisional regime is similar to the magnetic energy spectrum and thus different from what we observed for the collisionless regime. This fact may be understood in terms of the dissipative effects of the plasma resistivity that affect J, whose value is comparable to that of the plasma viscosity, determining the same dissipation length scale for J and U.

5. Conclusions

We have carried out an analysis of the turbulent cascade in the collisionless regime following a new perspective focused on the different structures observed in our numerical simulations that allowed us to shed light on the complex interplay between plasmoid and KH instabilities. Due to the presence of strong velocity shears, the plasmoid formation in collisionless regimes has to compete with the KH instability. The current sheets may disrupt into a plasmoid chain or into KH-driven vortices depending on the local behavior of the magnetic and velocity fields. This finding explains the discrepancy between the magnetic energy spectrum evaluated from the numerical simulations and the one we derived analytically under the assumption that the fully plasmoid-mediated turbulent regime has been achieved.

Appendix A
Magnetic versus Fluid Instability

We analyze the growth rate of reconnection and KH instabilities for a current-sheet-like equilibrium. Following Biskamp (2000), we assume sheared magnetic and velocity fields of the form

$$B_{\mathrm{eq}}(x) = B_{\mathrm{eq}}^0 \tanh(x), \qquad (A1)$$

$$V_{\mathrm{eq}}(x) = \frac{V_{\mathrm{eq}}^0}{\cosh^2(x)}. \qquad (A2)$$

We solve numerically the linearized version of the system of Equations (1)–(2) assuming $B_{\mathrm{eq}}^0 = 0.8$ and $V_{\mathrm{eq}}^0 = 1.0$. The results are summarized in Figure 11, where we show the growth rate for different cases: resistive tearing mode with $\eta = 3 \times 10^{-4}$ (as in Biskamp 2000), collisionless tearing mode with $d_e = 0.188$, and two cases of coexistence of velocity shear and resistive or collisionless reconnection. These values have been chosen imposing the condition $\gamma d_e^2 = \eta$ so that the linear growth rate of the tearing mode instability is the same in the purely resistive (blue curve) and collisionless (yellow curve) regimes.

We can see that the combined action of a sheared velocity field together with the sheared magnetic field in the collisionless regime gives a growth rate that is much higher than in all other cases. To our knowledge, this represents a new result that was previously overlooked. It is interesting that the spectrum of unstable modes broadens with respect to the purely collisionless tearing mode, but not as much as in the combined effect of KH and resistive tearing mode.

The effect of the presence of an equilibrium shear flow on the stability of resistive tearing modes has been studied in the past (Chen & Morrison 1990). Due to the freezing of the magnetic flux into the flow, valid in the ideal region where resistivity can be neglected, and being the standard stability parameter Δ' determined by the solution in this region, it is not
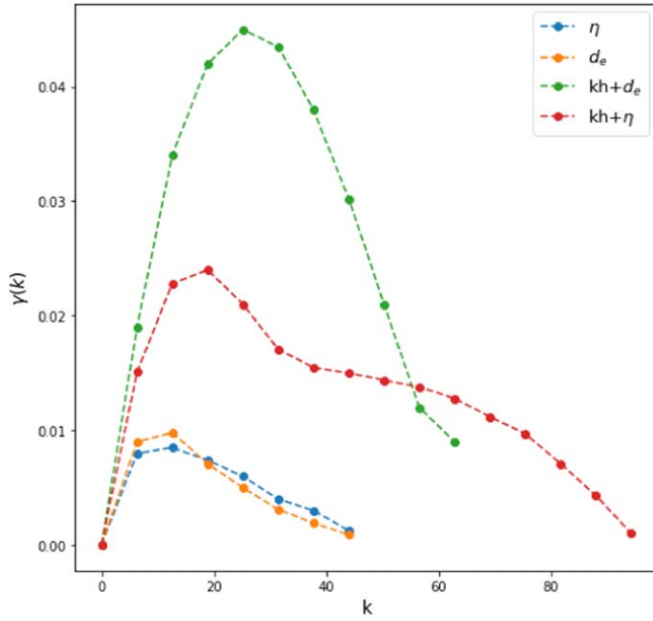
Figure 11. Growth rates γ as a function of the wavenumber for different cases: resistive (light blue) and collisionless (yellow) tearing modes with $\eta = 3 \times 10^{-4}$ and $d_e = 0.188$, respectively; combination of the KH mode with the resistive (green) and collisionless (red) tearing mode for the same parameters.

surprising that the presence of a shear flow can change the stability spectra for the tearing modes. The difference observed here, when considering the collisionless tearing mode, can be understood taking into account that in the high-k regime the growth rate of a collisionless tearing mode is proportional to d_e^3 (Biskamp 2000), which is very small. Hence these modes could be marginally stable and less influenced by the shear flow.

Moreover, we observe that the peak value is shifted to a higher k value. This result is relevant for the problem we are addressing here, where the evolution of current sheets in a turbulent environment is considered. Therefore, we may expect a stronger competition between magnetic reconnection and KH instability, unlike what happens in resistive regimes, where the current sheets in a turbulent environment are disrupted according to the plasmoid instability.

ORCID iDs

Dario Borgogno https://orcid.org/0000-0001-6831-1014
Daniela Grasso https://orcid.org/0000-0001-7522-3805
Massimiliano Romé https://orcid.org/0000-0003-3490-7949
Luca Comisso https://orcid.org/0000-0001-8822-8031

References

Baty, H. 2020, arXiv:2003.08660
Biskamp, D. 2000, Magnetic Reconnection in Plasmas (Cambridge: Cambridge Univ. Press)
Biskamp, D. 2003, Magnetohydrodynamic Turbulence (Cambridge: Cambridge Univ. Press)
Biskamp, D., & Welter, H. 1989, PhFlB, 1, 1964
Boldyrev, S., & Loureiro, N. F. 2017, ApJ, 844, 125
Carbone, V. 1995, PhRvE, 52, 1210
Carbone, V., Veltri, P., & Mangeney, A. 1990, PhFlA, 2, 1487
Cerri, S. S., & Califano, F. 2017, NJPh, 19, 025007
Chen, X. L., & Morrison, P. J. 1990, PhFlB, 2, 495
Comisso, L., Huang, Y.-M., Lingam, M., Hirvijoki, E., & Bhattacharjee, A. 2018, ApJ, 854, 103
Comisso, L., Lingam, M., Huang, Y.-M., & Bhattacharjee, A. 2017, ApJ, 850, 142
Comisso, L., Lingam, N., Huang, Y.-M., & Bhattacharjee, A. 2016, PhPl, 23, 100702
Comisso, L., & Sironi, L. 2018, PhRvL, 121, 255101
Comisso, L., & Sironi, L. 2019, ApJ, 886, 122
Comisso, L., Sobacchi, E., & Sironi, L. 2020, ApJL, 895, L40
Del Sarto, D., Califano, F., & Pegoraro, F. 2003, PhRvL, 91, 235001
Dong, C., Wang, L., Huang, Y.-M., Comisso, L., & Bhattacharjee, A. 2018, PhRvL, 121, 165101
Faganello, M., Califano, F., & Pegoraro, F. 2008, PhRvL, 101, 105001
Franci, L., Cerri, S. S., Califano, F., et al. 2017, ApJL, 850, L16
Furth, H. P., Killeen, J., & Rosenbluth, M. N. 1965, PhFl, 6, 459
Grasso, D., Borgogno, D., & Pegoraro, F. 2007, PhPl, 14, 055703
Grasso, D., Borgogno, D., Pegoraro, F., & Tassi, E. 2009, NPGeo, 16, 241
Grasso, D., Borgogno, D., Tassi, E., & Perona, A. 2020, PhPl, 27, 012302
Grasso, D., Pegoraro, F., Porcelli, F., & Califano, F. 1999, PPCF, 41, 1497
Harris, E. G. 1962, NCim, 23, 115
Huang, Y.-M., Comisso, L., & Bhattacharjee, A. 2017, ApJ, 849, 75
Huang, Y.-M., Comisso, L., & Bhattacharjee, A. 2019, PhPl, 26, 092112
Ji, H., & Daughton, W. 2011, PhPl, 18, 111207
Lazarian, A., Eyink, G., Vishniac, E., & Kowal, G. 2015, RSPTA, 373, 20140144
Loureiro, N. F., Schekochihin, A. A., & Uzdensky, D. A. 2013, PhRvE, 87, 013102
Mallet, A., Schekochihin, A. A., & Chandran, B. D. G. 2017, MNRAS, 468, 4862
Mininni, P. D., & Pouquet, A. 2009, PhRvE, 80, 025401
Ottaviani, M., & Porcelli, F. 1995, PhPl, 2, 4104
Politano, H., Pouquet, A., & Sulem, P. L. 1989, PhFlB, 1, 2330
Politano, H., Pouquet, A., & Sulem, P. L. 1995, PhPl, 2, 2931
Servidio, S., Dmitruk, P., Greco, A., et al. 2011, NPGeo, 18, 675
Servidio, S., Matthaeus, W. H., Shay, M. A., Cassak, P. A., & Dmitruk, P. 2009, PhRvL, 102, 115003
White, R. B. 1986, RvMP, 58, 183
Zhou, Y., Qin, H., Burby, J. W., & Bhattacharjee, A. 2014, PhPl, 21, 102109